RSC Advances

PAPER

View Article Online
View Journal | View Issue

Cite this: *RSC Adv.*, 2020, **10**, 41551

Fabrication of highly active phosphatase-like fluorescent cerium-doped carbon dots for *in situ* monitoring the hydrolysis of phosphate diesters†

Jinyan Du, * Shuangqing Qi, Juan Chen, Ying Yang, Tingting Fan, Ping Zhang, Shujuan Zhuo and Changqing Zhu*

Received 29th August 2020
Accepted 7th November 2020

DOI: 10.1039/d0ra07429b

rsc.li/rsc-advances

Ce-Doped carbon dots (CeCDs) were fabricated *via* a one-step hydrothermal carbonization using $Ce(NO_3)_3 \cdot 6H_2O$ and $EDTA \cdot 2H_2O$ as precursors, and various experimental techniques were employed to characterize the morphology, structure and composition of the as-obtained CeCDs. Using the disodium salt of bis(4-nitrophenyl)phosphate (BNPP) as a DNA model substrate, mimetic phosphatase activity toward phosphate ester hydrolysis cleavage was investigated. It was found that similar to the catalytic character of the natural enzyme, CeCDs as a hydrolase mimic can exhibit a good catalytic activity for promoting BNPP hydrolysis, in which metal Ce(III) acts as a center for binding and activation of the metal-bound hydroxide complex as well as a source of nucleophilic metal hydroxides. Additionally, based on the Inner Filter Effect (IFE), fluorescence spectra can be used to monitor the hydrolysis of BNPP using CeCDs, which mimic phosphatase. Thus, the unique properties of the CeCD mimetic phosphatases as well as the IFE sensing strategy would provide an ideal platform to monitor the catalytic phosphate ester hydrolysis processes. Finally, to validate the availability of the established catalytic systems, the CeCDs were further applied for degradation of organophosphorus pesticide chlorpyrifos. The degradation efficiency was estimated to be a satisfactory value of 74.50%, exhibiting a potential application prospect for treatment of the pollutants in the soil and water.

1. Introduction

Phosphate esters are crucial for cell division and growth, information storage and utilization, energy transduction, cellular signaling communication, and other biological processes in living systems.[1] Hydrolytic cleavage of the P–O linkage of phosphate esters is the key step for these processes.[2] Generally, phosphate esters are highly stable with a half-life up to thousands of years.[3] Fortunately, natural biological enzymes can hydrolyze the phosphate ester bond rapidly with a high catalytic performance and a high specificity.[4] However, poor stability and easy inactivation limit their large-scale applications.[5] Recently, fabrication of transition metal complexes as artificial hydrolytic metalloenzymes for facilitating phosphate diester hydrolysis has received considerable attention.[6–9] Investigations on Zn^{II},[10] Ni^{II},[11] Cu^{II},[12] Fe^{III},[13] Co^{II},[14] Mg^{II},[15] and Mn^{II} (ref. 16) complexes as hydrolytic metalloenzymatic models were successively reported. From a perspective of mechanism, these studies have shown that biological enzymes that catalyze the hydrolysis of phosphates are always activated by one, two or more metal ions of the transition metal complexes. It was believed that the metal ion can activate the phosphate group and a nucleophilic H_2O molecule, and stabilize the penta-coordinated phosphorus transition state by cooperative effect in metalloenzymes.[17] These mimetic metallohydrolases not only have similar natural enzyme activities and high substrate specificities, but also effectively overcome the disadvantages of natural enzymes, such as low stabilities due to denaturation, sensitivity to the environment, difficult preparation and purification, providing valuable information on the fundamental role of metal ions in promoting the hydrolysis reactions of phosphate ester.

In particular, the significant hydrolytic abilities of lanthanide metal have caused a widespread concern.[18–21] In comparison to biologically relevant transition metals or alkaline earth Lewis acids, trivalent metal ions like lanthanum(III) exhibit high catalytic activities toward P–O bond scission due to high Lewis acidity, oxidation state and charge density, coordination number, as well as fast ligand exchange rates.[22,23] Cerium is a special among lanthanides because it can form a tetravalent oxidation state under aqueous solutions. Ce(IV) ion has been found to possess striking activity in promoting bis(4-nitrophenyl) phosphate (BNPP) hydrolysis, which was

Anhui Key Laboratory of Chemo-Biosensing, Key Laboratory of Functional Molecular Solids, Ministry of Education, College of Chemistry and Materials Science, Anhui Normal University, Wuhu, 241000, P. R China. E-mail: dujinyn@mail.ahnu.edu.cn; zhucq@mail.ahnu.edu.cn

† Electronic supplementary information (ESI) available. See DOI: 10.1039/d0ra07429b

attributed to the ability of Ce(IV) to form covalent bonds with phosphate substrates and promote the formation of penta-coordinate intermediates.[24,25] Many Ce(IV)-based mimetic hydrolase models have been applied in the study of phosphate ester hydrolysis. It was reported that using remarkable specificity of Ce(IV)/EDTA complex, gap-site in substrate DNA can be selectively hydrolyzed.[26] Moreover, the dicerium complexes were proved to be able to carry out the double strand hydrolysis of DNA.[27] Recently, Ceria (CeO_2) nanocrystals were served as mimic phosphatases for cleaving the phosphate ester bond in *para*-nitrophenyl phosphate.[28] However, owing to the poor water-solubility and complicated synthesis-processing of these complexes containing metallomicelles or macrocyclic ligand, the application of these artificial hydrolytic metalloenzymes catalytic systems is largely restricted.

Fortunately, fluorescent carbon dots (CDs) with the advantages of optimal size, biocompatibility, and good photo- or electro-catalytic efficiency,[29] have been applied in many fields including bioimaging and sensing, nanomedicine, optoelectronic devices, ion detection and catalysis.[30] More and more carbon-based nanomaterials were demonstrated to hold an intrinsic enzyme-like activity.[31] Hitherto, most of the catalytic reactions of nanozymes are based on peroxidase,[32,33] oxidase,[34,35] laccase,[36,37] and catalase,[38,39] *etc.* However, artificial hydrolases based on carbon nanomaterial are also highly desirable.

Herein, based on high sensitivities of P–O bond cleavage toward lanthanide ions and fluorescence properties of CDs, we have successfully synthesized fluorescent Ce-doped CDs (CeCDs) by a one-step hydrothermal method using EDTA as a carbon source and $Ce(NO_3)_3$ as a Ce dopant. We used hydrolysis of phosphate diester as a model reaction for the cleavage of phosphorus bond of DNA and RNA.[40] Here, BNPP was chosen as a DNA model substrate, and phosphatase-like activity of the obtained CeCDs was explored based on the inner filter effect (IFE), *i.e.*, the maximum absorption range of BNPP hydrolysis products (*p*-nitrophenol) partly overlaps with emission spectrum of the as-prepared CeCDs, resulting in an efficient fluorescence quenching of the CeCDs. The rate of BNPP hydrolysis was calculated and the possible catalytic mechanism was proposed. Our results suggested that the fluorescence CeCDs can promote and monitor the process of phosphate ester hydrolysis cleavage. Finally, the CeCDs was further applied to degradation of organophosphorus pesticide chlorpyrifos. Within 48 h, the degradation efficiency was estimated to be 74.50%.

2. Experiments

2.1 Materials and reagents

Cerium(III) nitrate hexahydrate ($Ce(NO_3)_3 \cdot 6H_2O$, 99.99%, Adamas), ethylenediaminetetraacetic acid disodium salt dihydrate ($EDTA \cdot 2H_2O$, 98%) was acquired from Guoyao Chemical Reagent Company (Shanghai, China), BNPP was prepared from the commercial product purchased from Sigma. Chlorpyrifosv (>99%) was obtained from Aladdin. Tetracosane, acetone, ethyl acetate and trichloromethane were obtained from Aladdin. All chemical reagents were used without any treatment. All solutions were prepared with ultrapure water (18.25 MΩ cm).

2.2 Apparatus

The morphology of the as-prepared CeCDs was characterized by transmission electron microscopy (TEM, JEOL 2010, Japan). X-ray photoelectron spectroscopy (XPS) was employed to investigate the content of elements and the conformation of the CeCDs was determined by Thermo Scientific K-Alpha instrument. Elemental analysis was carried out by energy dispersive X-ray spectroscopy (EDS) conducted at the accelerating voltage of 200 kV on a Philips S-4800 instrument. UV-vis spectra of the samples were obtained on a Hitachi UV-2910 spectrophotometer. The fluorescence spectra were recorded with an Edinburgh FS5 fluorescence spectrophotometer. Fourier transform infrared (FTIR) spectra were carried out on a PerkinElmer PE-983 FTIR spectrophotometer. The degradation of chlorpyrifos was employed by Gas Chromatography-Mass Spectrometer (GC-MS Thermo Trace-1300 ISQ-Mass). Phosphate ion were quantified using a ICS-1100 ion chromatography (Thermo, USA) equipped with an AS11-HC column (250 mm × 4 mm) and a conductivity detector (883 Basic IC plus 1). The mobile phase was 30 mM sodium hydroxide at a flow rate of 1.2 ml min^{-1} and the injection volume of 25 μl.

2.3 Preparation of CeCDs

The CeCDs were synthesized by a hydrothermal method. Typically, 1.0000 g of $EDTA \cdot 2H_2O$ and 2.3451 g of $Ce(NO_3)_3 \cdot 6H_2O$ were dispersed in 30 ml ultrapurewater under magnetic stirring to form a transparent solution. Afterward, the mixture solution was transferred into a 50 ml Teflon equipped stainless steel autoclave and heated at 180 °C for 6 h. After the resultant solution was cooled to room temperature naturally, the transparent yellow solution was filtered and as-collected supernatant was further dialyzed in the dialysis bag (molecular weight: 1000 kDa) for 24 h to remove the excess reactants. The purified CeCDs (concentration: 15.8 mg ml^{-1}) were preserved at 4 °C for the following experiments.

2.4 Phosphatase activity of CeCDs

The disodium salt of BNPP was used as a DNA model substrate to investigate phosphodiesterase activity. Commonly, in the presence of phosphatase, BNPP was transformed into *p*-nitrophenol which induced the increase in the absorption of the band at 400 nm. Here, the as-prepared CeCDs were deemed as artificial phosphatases to investigate the catalytic activity of BNPP hydrolytic cleavage. In a typical experiment, 1.0 ml BNPP solution (5 mM), 0.5 ml CeCDs and 1.0 ml Tris–HCl buffer were introduced into a colorimetric tube. The color of the solution changed gradually from transparent to yellow as the reaction proceeding. The process of BNPP hydrolysis was detected spectrophotometrically by monitoring the time evolution of *p*-nitrophenol (λ_{max} = 400 nm) through a wavelength scan from 200 to 900 nm at 25 °C, containing 100 equivalents of substrate relative to the catalyst, until roughly 2% reaction conversion was

reached. Comparative experiments in the absence of the CeCDs were carried out under identical conditions.

2.5 Degradation of pesticide

The degradation rate of pesticides catalyzed by CeCDs in acetone was measured by GC-MS, using chlorpyrifos as an external standard. Specific operations and implementation processes are detailedly described in ESI.†

3. Results and discussion

3.1 Characterization of CeCDs

The CeCDs were synthesized according to the protocol described in the experimental section. The structure and morphology of the CeCDs were analyzed using TEM. Fig. 1A clearly shows that the resulted CeCDs are well mono-dispersed. The high resolution transmission electron microscopy (HRTEM) image (inset in Fig. 1A) displays a lattice fringe spacing of 0.31 nm, which is attributed to the (002) spaces of graphitic carbon.[41] The size distribution ranges from 1.9 nm to 3.5 nm (Fig. 1B) with an average size of around 2.7 nm (100 nanoparticles were counted), which is larger than that of the Ce-free bare CDs (an average diameter 2.3 nm, Fig. S1†).

As shown in Fig. 1C, optical absorption in the UV region was observed in the UV-vis absorption spectrum of CeCDs. The CeCDs have two strong peaks at 250 and 280 nm, corresponding to π–π* and n–π* transitions, respectively.[42,43] From the inset of Fig. 1C, it was observed that the CeCDs were yellow liquid illuminated with ambient light, and the CeCDs emitted bright blue light under the UV light excitation (365 nm). Fig. 1D demonstrates the emission spectra of CeCDs excited by the light of wavelength ranging from 320 to 400 nm. The as-prepared CeCDs have the strongest emission at 426 nm when excited at 350 nm (λ_{ex}). It could also be observed that the CeCDs exhibit excitation-independent emission properties (the fluorescent emission spectra of Ce-free bare CDs is shown in Fig. S2† for comparison), which could be attributed to the homogeneous surface structure, and monodispersity of the CeCDs.[44,45] In addition, the average fluorescence quantum yield (QY) of the CeCDs in aqueous solution at room temperature was measured to be 27% using quinine sulfate as a reference (QY of quinine sulfate is 54% at 350 nm excitation wavelength), which is comparable with that in the previous reported CDs.[46] However, the QY of the Ce-free bare CDs was only 13%, lower than that of the CeCDs. The results indicate that the introduction of metal Ce dramatically improves fluorescent performance of CDs.[47]

The FTIR spectrum of the CeCDs is shown in Fig. 2A. Remarkably, the peak emerges at 3440 cm^{-1}, corresponding to the stretching vibration of O–H. The peak at 1679 cm^{-1} is attributed to C=O stretching vibration, and the stretching vibration bands of C–O at 929 and 728 cm^{-1} indicate the presence of carboxylic acid and other oxygen-containing functional groups. The absorbance at 1630 cm^{-1} is assigned to N–H bending vibration, suggesting the existence of amino-containing functional groups. These peaks suggest that the CeCDs have logical hydrophilic properties as well as significant stability and dispersibility in water.[48]

The elemental composition of the CeCDs was analyzed using X-ray spectroscopy (EDS). EDS spectrum of the CeCDs presents five elements of C, N, O, Ce and Na from 0 to 10 keV (Fig. S3†), in

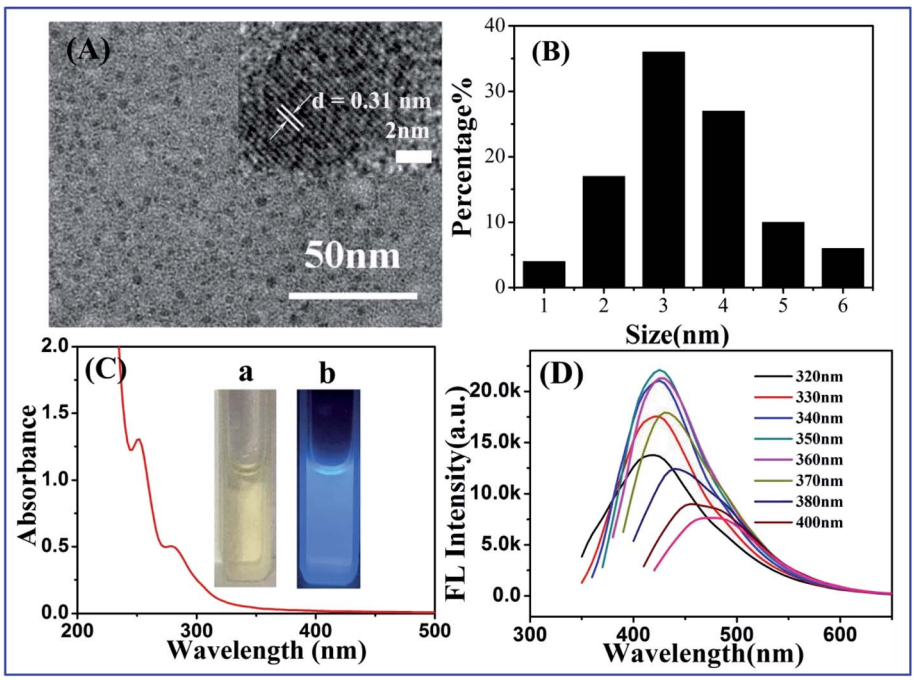

Fig. 1 (A) TEM and HRTEM (inset) images. (B) Size distribution of the as-prepared CeCDs. (C) UV-vis absorption spectra of the CeCDs solution. Inset: (a) Photograph of CeCDs illuminated with ambient light, (b) photograph of CeCDs under UV light (365 nm). (D) Fluorescence emission spectra of the CeCDs dispersed in water (ex: 320–400 nm, em: 350–650 nm).

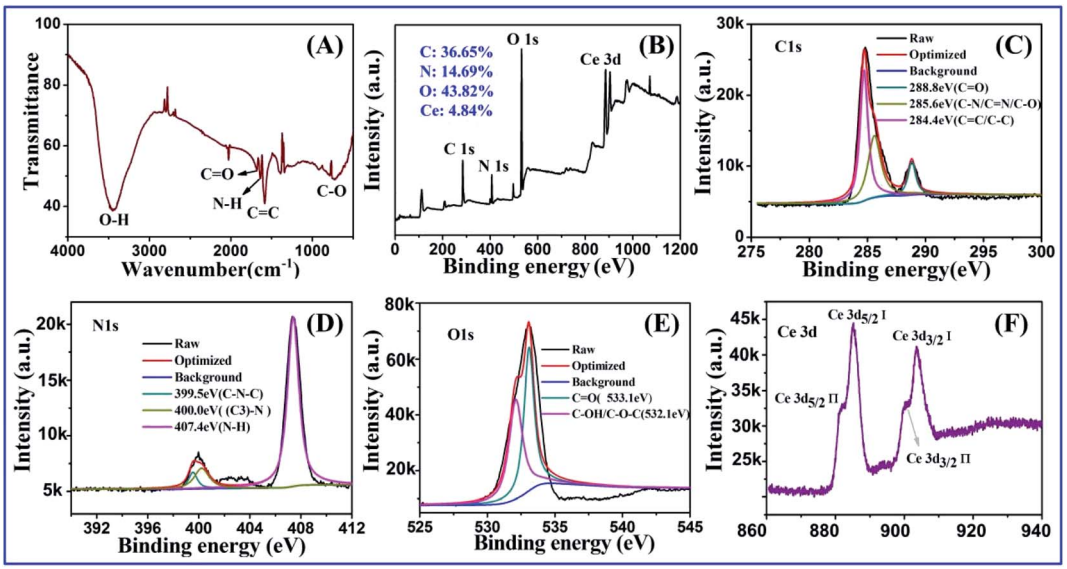

Fig. 2 (A) FTIR spectrum, (B) XPS entirety and high-resolution survey of (C) C 1s, (D) N 1s, (E) O 1s and (F) Ce 3d of the CeCDs.

good agreement with those of the precursors. Moreover, the XPS spectrum analysis show that C_{1s}, N_{1s}, O_{1s} and Ce_{3d} peaks locate at 284.4, 407.4, 532.1 and 890.0 eV (Fig. 2B), respectively. Since there are no other carbon sources, carbon elements in the CeCDs must be from the EDTA, while nitrogen and cerium are from the introduction of $Ce(NO_3)_3$.[49] The high resolution XPS spectrum of C_{1s} exhibits C=C/C–C, C–O/C–N/C=N, C=O main peaks at the corresponding binding energies of 284.4, 285.6 and 288.8 eV (Fig. 2C).[50] In the high-resolution region of N_{1s} as shown in the Fig. 2D, there are three peaks residing at 399.5, 400.0 and 407.4 eV, which are attributed to the C–N–C, (C3)–N, N–H groups, respectively.[45] The O_{1s} spectrum can be resolved as follows: C=O is at 533.1 eV, C–OH/C–O–C is at 532.1 eV (Fig. 2E).[51] The Ce 3d spectrum consists of four characteristic peaks (Fig. 2F). The peaks at 903.9 and 899.6 eV are ascribed to the binding energy of Ce $3d_{3/2}$ orbital, while the peaks at 885.6 and 881.1 eV correspond to the binding energy of Ce $3d_{5/2}$ orbital. Besides, the peak positions of the Ce 3d orbitals and the binding energy difference (ΔE) between these two components were approximate, indicative of an identical 3+ valence state of Ce.[52,53] In addition, the FTIR and XPS show that there are rich oxygen-containing groups and amino groups on the surface of the CeCDs, indicative of a good hydrophilicity.[54–56] This facilitates catalytic hydrolysis of BNPP.

3.2 Optimization of synthesis and hydrolysis conditions for phosphatase-like activity of CeCDs

The phosphatase-like activity of CeCDs was investigated by employing the substrate BNPP in aqueous solution. Hydrolysis product of BNPP, *p*-nitrophenol, exhibits distinct optical absorption properties (λ_{max} = 400 nm), making it possible to track the reaction progress by using absorbance spectroscopic means. Fig. 3 shows the UV-vis spectra through a wavelength scan from 300 to 600 nm collected in the process of hydrolytic cleavage of BNPP in the presence of CeCDs, Ce-free bare-CDs and no catalyst after incubation for 3 h at 25 °C. No obvious absorption at 400 nm was observed when Ce-free bare CDs were served as the catalyst or no catalyst was presented for the hydrolytic cleavage of BNPP. At variance, in the presence of CeCDs, remarkable absorption peak at 400 nm was caught along with the appearance of light yellow color (c of inset in Fig. 3). These results clearly demonstrate that the CeCDs have an obvious phosphatase-like activity.

It was found that several factors, including concentration of cerium source in combination with EDTA, temperature and time of the reaction, can affect phosphatase-like activity of the CeCDs. To optimize the synthesis conditions of the CeCDs, first, the ratio of EDTA to cerium nitrate was controlled from 0.15 to 0.75, maintaining other parameters such as reaction time (4 h) and temperature (200 °C) as constants. After purification, the CeCDs with different ratio of EDTA to cerium nitrate were added to 1 ml BNPP (5 mM) for incubation 2 h at 25 °C. The absorbance increase value of the *p*-nitrophenol band at 400 nm was

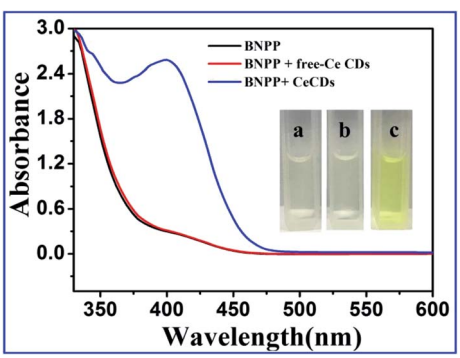

Fig. 3 The UV-vis absorption spectra for BNPP, BNPP + Ce-free bare CDs and BNPP + CeCDs solution after incubation for 3 h at 25 °C. Inset: The photograph of the corresponding system under ambient conditions: (a) BNPP, (b) BNPP + Ce-free bare CDs, (c) BNPP + CeCDs.

selected as a standard for evaluating phosphatase-like performance, which is also a criterion for evaluating optimization of the following other synthesis conditions. As is observed in Fig. S4A,† at the optimum ratio of 0.5 between EDTA and cerium nitrate, the CeCDs show the highest catalytic properties. Then, the effect of reaction temperature on the catalytic properties of as-synthesized CeCDs was also investigated. The reaction temperature increases in a step of 20 from 140 to 220 °C with fixing the ratio of EDTA to cerium nitrate of 0.5. The results indicate that the CeCDs synthesized at 200 °C exhibit a higher phosphatase-like activity (Fig. S4B†). Similarly, the duration of the reaction was also adjusted to estimate the optimum reaction time. As illustrated in Fig. S4C,† the CeCDs synthesized with 6 h reaction display the highest catalytic activity, implying that 6 h of reaction time is the optimum experimental condition. Therefore, under the optimal conditions (*i.e.*, the ratio of EDTA to cerium nitrate: 0.5, reaction temperature: 200 °C, reaction time: 6 h), a facile carbonization and efficient Ce-doping occurs to generate the CeCDs with appreciable phosphatase-like activity.

Then, the pH of BNPP hydrolysis was optimized in the range of 5–10 in Tris–HCl (0.05 M) buffer solution. As shown in Fig. S5,† the catalytic cleavage activity of CeCDs for BNPP hydrolysis shows the best performance in pH 8.2–8.7. Therefore, in the subsequent experiments, pH 8.5 was used as the optimal condition for BNPP hydrolysis.

3.3 Catalytic kinetics and indication process for BNPP hydrolysis

The efficiency of CeCDs for hydrolytic cleavage of BNPP in aqueous solution was determined spectrophotometrically by monitoring the time evolution of *p*-nitrophenol ($\lambda_{abs} = 400$ nm) through a wavelength scan from 300 to 600 nm at 25 °C, until roughly 2% reaction conversion was reached. The absorbance spectra of BNPP upon the addition of CeCDs were shown in Fig. 4A, where the spectra were recorded at 10 min intervals for 2 h. From the Fig. 4A, the absorption at 400 nm increases gradually with the appearance of yellow solution. The pseudo-first-order-rate constants of BNPP hydrolysis, $k_{cat} = 1.84 \times 10^{-3}$ min^{-1} (error $= 3.89 \times 10^{-5}$), were obtained directly from the plot of $\log[A_\infty/(A_\infty - A_t)]$ values *versus* time t (Fig. 4B, $R^2 = 0.9978$), where A_∞ is the absorbance at 400 nm after incubation 2 days at 25 °C, A_t is the absorbance of 400 nm at time t.[57,58] The release of the first *p*-nitrophenol molecule from BNPP is the rate-determining step in the BNPP catalytic hydrolysis. Therefore, apparent rate constant, k_{obs}, is almost equal to the first order rate constant, k_{cat}.[18] For comparison, the same concentration of Ce-free bare CDs was added to BNPP substrate, then the absorption spectra were measured at 20 min intervals for 2 h. From the Fig. S6,† there was no obvious change in the absorption spectrum. The results on the one hand indicate that, Ce-free bare CDs have no significant catalytic activity for the hydrolysis of BNPP, and on the other hand, the element Ce is essential and plays a vital role in catalyzing the hydrolysis of BNPP.

In order to eliminate the possibility of photocatalysis, the absorbance spectra of BNPP upon the addition of CeCDs under dark conditions were presented in Fig S7.† It can be observed that there is a significant increase in absorption at 400 nm within 120 min. From the plot of $\log[A_\infty/(A_\infty - A_t)]$ values *versus* time t (Fig. S7B,† $R^2 = 0.9950$), the pseudo-first-order-rate constant of BNPP hydrolysis was calculated to be $k_{cat} = 2.6 \times 10^{-3}$ min^{-1} (error $= 5.5 \times 10^{-5}$), which is basically equal to that of under sunlight. These results indicate that photocatalysis is not responsible for the hydrolysis of BNPP, thus the CeCDs indeed serves as a mimic enzyme in the hydrolysis reaction. Furthermore, potassium persulfate was added to the catalytic system as an electron scavenger, and the absorption spectra were recorded (Fig. S8A†). It can be observed that the absorption at 400 nm increases gradually, and the calculated pseudo-first-order-rate constant of BNPP hydrolysis, $k_{cat} = 2.5 \times 10^{-3}$ min^{-1} (error $= 3.02 \times 10^{-4}$), is consistent with the result without adding potassium persulfate (Fig. S8B†), indicating that there was no electron transfer in the catalytic process.

To further understand the acceleration behavior of CeCDs on the hydrolysis of BNPP, the fluorescence emission spectra of the CeCDs were determined in the presence of different concentration BNPP. As shown in Fig. S9,† the fluorescence intensities of the CeCDs decrease with the increase in BNPP concentration. This observation indicates a strong binding between the CeCDs and BNPP molecules, which leads to the photoelectron transfer from BNPP to the CeCDs.[59] Because oxygen atom of the BNPP

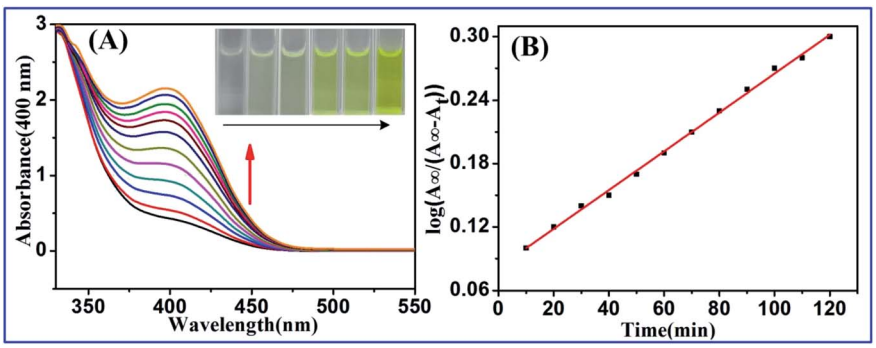

Fig. 4 (A) Time-dependent UV-vis spectral changes in BNPP solution catalyzed by CeCDs. The spectra were recorded at intervals of 10 min. The inset is the color change of photographs of BNPP solution in the presence of CeCDs in natural light. (B) Plots of $\log[A_\infty/(A_\infty - A_t)]$ *versus* time for the catalytic hydrolytic cleavage of BNPP at room temperature.

molecule has a strong affinity to metallic ions, the phosphoryl oxygen of BNPP molecule may bond with the metal ion (Ce(III)) of CeCDs when the BNPP was added into the CeCDs solution, which is proved by the obvious change of fluorescence intensity of the CeCDs in Fig. S9.† This situation could promote the formation of the reaction intermediate with BNPP and the metal-bound hydroxide activation, which can facilitate an intramolecular nucleophilic reaction. As is known, the reaction rate of intramolecular reactions can be considerably enhanced compared with that of intermolecular reactions.[60] Thus, because of the synergic effects of Ce(III) ion and metal hydroxide activation, the P–O bond of BNPP molecule can be cleaved more favorably.

According to the above analysis, the possible reaction mechanism for the catalytic hydrolysis of BNPP was proposed as shown in Scheme 1. In the step 1, due to a good hydrophilicity, the metal Ce on the surface of CeCDs in aqueous solution are favorably bonded with water molecules. Under alkaline conditions, the deprotonation of the metal-bound water forms a nucleophilic metal hydroxide. In the step 2, the intermediate (R) is formed by coordination of the oxygen atom of BNPP with the aqua-hydroxyl active species, which is beneficial to the transformation of an intermolecular reaction into an intramolecular one. In the step 3, intramolecular metal hydroxides attack the positive-charged P atoms of the BNPP molecule, promoting the release of *p*-nitrophenol and production of phosphate monoester with first-order-rate constant (the rate-determining step). And in the step 4, *p*-nitrophenyl phosphate (NPP), which is one of the products of BNPP hydrolysis in the above step, rapidly releases phosphoric acid and another *p*-nitrophenol and simultaneously regenerates the active species of step 1 (the product of phosphate ion has been caught by ion chromatography, see Fig. S10†). Ultimately, when another BNPP molecule is associated with the regenerated metal hydroxide, the catalytic process begins to recycle. Our proposed mechanism is similar to that of BNPP hydrolysis catalyzed by lanthanide or transition metalloenzymes.[61]

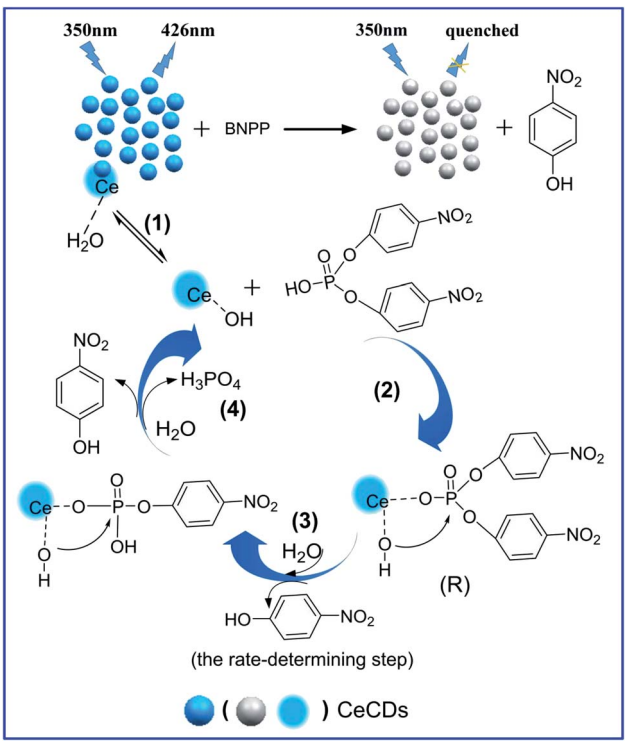

Scheme 1 Schematic illustration of catalytic hydrolysis cleavage mechanism of BNPP catalyzed by the fabricated CeCDs.

The phosphatase catalytic behavior of CeCDs was further investigated according to the steady-state kinetic analysis using BNPP as the substrate. The kinetic data were obtained by varying substrate concentration while keeping the other substrate concentration constant.[62,63] It can be observed in Fig. S11A† that the hydrolytic reaction of phosphate ester catalyzed by the CeCDs was heavily dependent on the concentration of substrate which followed a typical Michaelis–Menten behavior towards BNPP.[64] Hence, a series of catalytic reaction parameters could be calculated according to the Line weaver–Burk double reciprocal plot (Fig. S11B†) based on the equation: $1/v = (K_m/V_{max}) \times (1/[S]) + 1/v_{max}$, where v is the initial reaction velocity, K_m is the Michaelis–Mentenconstant, v_{max} is the maximum reaction velocity, and [S] is the concentration of substrates. In Table S1,† we compare our kinetic parameters result to those reported in the literatures on the other catalysts. The apparent K_m value of CeCDs with BNPP as the substrate (0.866 mM) is lower than that of metal complexes for mimetic phosphate hydrolases, suggesting that the CeCDs is an excellent mimetic hydrolase with a higher affinity.[65,66]

Simultaneously, we measured the fluorescence behavior of CeCDs upon the addition of BNPP until roughly 2% reaction conversion was reached, where the spectra were recorded for 2 hours at 10 min intervals. As shown in Fig. 5A, the fluorescence of CeCDs was gradually quenched with the appearance of dark blue color, corresponding to the increase of absorption peak at 400 nm in UV-vis absorption spectra (Fig. 4A). This scenario could provide a basis for quantitative monitoring of the catalytic hydrolytic cleavage of BNPP. In order to comprehend the fluorescence quenching mechanism of CeCDs, the emission spectra of CeCDs were found to overlap partially with the absorption spectra of *p*-nitrophenol (Fig. S12†). Note that *p*-nitrophenol can shield the emission light of the CeCDs, therefore, the fluorescence quenching mechanism may be regarded as fluorescence resonance energy transfer (FRET) or IFE.[67,68] However, the fact that there is no change in the fluorescence lifetime (Fig. S13†) of CeCDs before and after adding BNPP indicates that no FRET process occurs between CeCDs and *p*-nitrophenol. These results suggest that the highly efficient IFE is the dominant reason for the fluorescence quenching of CeCDs in the catalytic system.

Moreover, the rate constants of the catalytic hydrolytic cleavage of BNPP was calculated from the fluorescence spectra of the CeCDs mimetic hydrolase.[69] The plot of $\log[F_0/(F_0 - F_t)]$ *versus* time t was shown in Fig. 5B. Here, F_0 is the initial fluorescence intensity of the CeCDs at maximum emission, and F_t represents the fluorescence intensity of the CeCDs at maximum emission at time t. The rate constant (k_{cat}) of BNPP hydrolysis calculated from the linear relationship of $\log[F_0/(F_0 - F_t)]$ *versus* time t was 1.33×10^{-3} min^{-1}, which is approximately

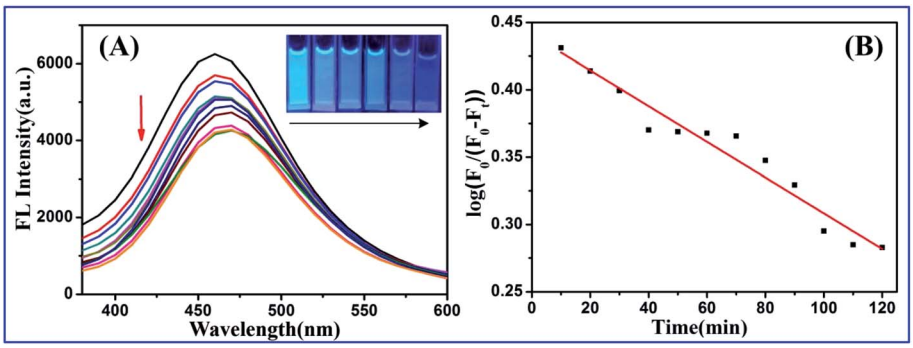

Fig. 5 (A) Time-dependent fluorescence emission spectral changes of the CeCDs in BNPP solution. The spectra were recorded at intervals of 10 min, excitation wavelength = 350 nm. The inset is the fluorescence color photographs of CeCDs solution in the presence of BNPP under a 365 nm UV lamp. (B) Plots of $\log[F_0/(F_0 - F_t)]$ *versus* time for the catalytic hydrolytic cleavage of BNPP at room temperature.

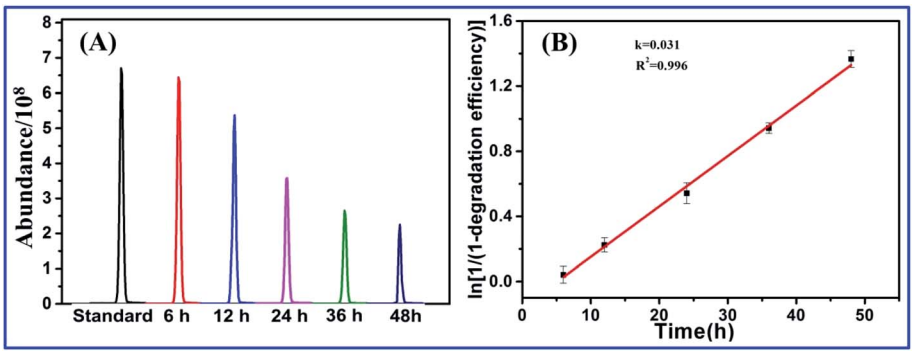

Fig. 6 (A) Time-dependent GC-MS chromatogram of chlorpyrifos samples upon addition of the CeCDs. Retention time: 19.91 min. (B) Plots of ln [1/(1 − degradation efficiency)] *versus* time for the catalytic degradation of chlorpyrifos at room temperature.

consistent with the values calculated from relative intensity of absorbance. All of the experimental results suggest that the catalytic hydrolysis process of BNPP can be monitored by the fluorescence behavior of mimic enzyme itself. Therefore, it is undoubtedly convenient for a class of reaction without specific spectrophotometric characteristics of the substrates.

3.4 Pesticide chlorpyrifos degradation

To validate the availability of the established catalytic systems, the CeCDs were further applied for the degradation of pesticide chlorpyrifos. The degradation rate of chlorpyrifos was analyzed by GC–MS using chlorpyrifos as the external standard. As shown in Fig. 6A, the peak area values are along with a significant decrease within 48 h. The natural logarithm of the concentration of chlorpyrifos *vs.* time was plotted (Fig. 6B). The first order rate constant was calculated to be 3.1×10^{-2} h ($R^2 = 0.996$), indicative of an excellent degradability of CeCDs for chlorpyrifos.[70] The degradation rate of chlorpyrifos by CeCDs within 48 h was 74.50% (Table S2†). Herein, the degradation percentage of chlorpyrifos was obtained according to the following formula:[71] Percentage of chlorpyrifos degradation = (peak area of initial concentration chlorpyrifos − peak area of chlorpyrifos)/peak area of initial concentration chlorpyrifos. As a comparison, degrading chlorpyrifos catalyzed by Ce-free bare CDs was also investigated. As shown in Fig. S14,† the change in peak area was negligible, indicating that the Ce-free bare CDs have no obvious catalytic performance for the chlorpyrifos degradation. These results again verify that the element of Ce is indispensable for cleavage of the P–O bond.

4. Conclusion

In summary, we have prepared water-soluble, fluorescent CeCDs by a facile one-step hydrothermal method using EDTA as a carbon source and $Ce(NO_3)_3$ as a Ce dopant. Using BNPP as a DNA model substrate, phosphatase-like activity of the as-obtained CeCDs were systematically investigated. On the one hand, a highly catalytic performance toward BNPP hydrolysis was found due to the synergistic effect of Ce(III) ion and metal hydroxide activation; on the other hand, IFE leads to fluorescence change of the CeCDs mimetic hydrolase in the process of BNPP hydrolysis. Moreover, the values of the rate constants calculated from the absorbance change of *p*-nitrophenol are primarily consistent with those from the fluorescence intensity change of CeCDs mimetic hydrolase. These unique properties would provide an ideal platform for *in situ* monitoring the catalytic process of hydrolysis of phosphate diester.

Conflicts of interest

There are no conflicts to declare.

Acknowledgements

This work was financially supported by the National Natural Science Foundation of China (no. 21705003) and Education Natural Science Research Foundation, Anhui Province, China (no. KJ2017A310).

References

1 J.-q. Xie, B.-y. Jiang, X.-m. Kou, C.-w. Hu, X.-c. Zeng and Y.-t. Li, *Transition Met. Chem.*, 2003, **28**, 782–787.
2 A. Tsubouchi and T. C. Bruice, *J. Am. Chem. Soc.*, 1995, **117**, 7399–7411.
3 N. H. Williams, B. Takasaki, M. Wall and J. Chin, *Acc. Chem. Res.*, 1999, **32**, 485–493.
4 X. Wei, Y. Hu, B. S. Razavi, J. Zhou, J. Shen, P. Nannipieri, J. Wu and T. Ge, *Soil Biol. Biochem.*, 2019, **131**, 62–70.
5 J. Song, P. Su, Y. Yang and Y. Yang, *New J. Chem.*, 2017, **41**, 6089–6097.
6 J. C. Lewis, *ACS Catal.*, 2013, **3**, 2954–2975.
7 F. Gao, C. Yin and P. Yang, *Chin. Sci. Bull.*, 2004, **49**, 1667–1680.
8 E. Y. Tirel, Z. Bellamy, H. Adams, V. Lebrun, F. Duarte and N. H. Williams, *Angew. Chem., Int. Ed.*, 2014, **53**, 8246–8250.
9 J. A. Cowan, *Chem. Rev.*, 1998, **98**, 1067–1088.
10 R. Sanyal, A. Guha, T. Ghosh, T. K. Mondal, E. Zangrando and D. Das, *Inorg. Chem.*, 2014, **53**, 85–96.
11 O. V. Amirkhanov, O. V. Moroz, K. O. Znovjyak, T. Y. Sliva, L. V. Penkova, T. Yushchenko, L. Szyrwiel, I. S. Konovalova, V. V. Dyakonenko, O. V. Shishkin and V. M. Amirkhanov, *Eur. J. Inorg. Chem.*, 2014, **2014**, 3720–3730.
12 R. E. H. M. B. Osório, R. A. Peralta, A. J. Bortoluzzi, V. R. de Almeida, B. Szpoganicz, F. L. Fischer, H. Terenzi, A. S. Mangrich, K. M. Mantovani, D. E. C. Ferreira, W. R. Rocha, W. Haase, Z. Tomkowicz, A. d. Anjos and A. Neves, *Inorg. Chem.*, 2012, **51**, 1569–1589.
13 D.-f. Li, Z.-r. Liao, Y.-g. Wei, F. Du, M. Wang, W.-x. Chen, W.-k. Li and X.-a. Mao, *Dalton Trans.*, 2003, 2164–2169.
14 T. Humphry, M. Forconi, N. H. Williams and A. C. Hengge, *J. Am. Chem. Soc.*, 2002, **124**, 14860–14861.
15 T.-a. Okamura, R. Furuya and K. Onitsuka, *J. Am. Chem. Soc.*, 2014, **136**, 14639–14641.
16 R. Van Gorkum, J. Berding, A. M. Mills, H. Kooijman, D. M. Tooke, A. L. Spek, I. Mutikainen, U. Turpeinen, J. Reedijk and E. Bouwman, *Eur. J. Inorg. Chem.*, 2008, **2008**, 1487–1496.
17 M. M. Aboelnga and S. D. Wetmore, *J. Am. Chem. Soc.*, 2019, **141**, 8646–8656.
18 F.-z. Li, F. Feng, L. Yu and J.-q. Xie, *J. Solution Chem.*, 2014, **43**, 1331–1343.
19 T. Gunnlaugsson, R. J. H. Davies, M. Nieuwenhuyzen, C. Stevenson, R. Viguier and S. Mulready, *Chem. Commun.*, 2002, 2136–2137.
20 P. Gomeztagle and A. K. Yatsimirsky, *Inorg. Chem.*, 2001, **40**, 3786–3796.
21 F. Feng, S. Cai and F. Liu, *J. Dispersion Sci. Technol.*, 2016, **37**, 352–359.
22 H.-l. Shang, L. Yu, S. Li and J.-q. Xie, *J. Dispersion Sci. Technol.*, 2014, **35**, 411–417.
23 S. J. Franklin, *Curr. Opin. Chem. Biol.*, 2001, **5**, 201–208.
24 M. Komiyama, N. Takeda and H. Shigekawa, *Chem. Commun.*, 1999, 1443–1451.
25 R. A. Moss, *Chem. Commun.*, 1998, 1871–1872.
26 Y. Yamamoto, A. Uehara, T. Tomita and M. Komiyama, *Nucleic Acids Res.*, 2004, **32**, e153.
27 W. Chen, Y. Kitamura, J.-M. Zhou, J. Sumaoka and M. Komiyama, *J. Am. Chem. Soc.*, 2004, **126**, 10285–10291.
28 M. J. Manto, P. Xie and C. Wang, *ACS Catal.*, 2017, **7**, 1931–1938.
29 X. Xu, R. Ray, Y. Gu, H. J. Ploehn, L. Gearheart, K. Raker and W. A. Scrivens, *J. Am. Chem. Soc.*, 2004, **126**, 12736–12737.
30 J. Zhao, F. Li, S. Zhang, Y. An and S. Sun, *New J. Chem.*, 2019, **43**, 6332–6342.
31 X. Shan, L. Chai, J. Ma, Z. Qian, J. Chen and H. Feng, *Analyst*, 2014, **139**, 2322–2325.
32 W. Shi, Q. Wang, Y. Long, Z. Cheng, S. Chen, H. Zheng and Y. Huang, *Chem. Commun.*, 2011, **47**, 6695–6697.
33 S. Li, X. Zhao, R. Gang, B. Cao and H. Wang, *Anal. Chem.*, 2020, **92**, 5152–5157.
34 Y. Wang, Y. Yang, W. Liu, F. Ding, P. Zou, X. Wang, Q. Zhao and H. Rao, *Mikrochim. Acta*, 2019, **186**, 246.
35 S. Zhuo, J. Fang, M. Li, J. Wang, C. Zhu and J. Du, *Mikrochim. Acta*, 2019, **186**, 745.
36 H. Li, S. Guo, C. Li, H. Huang, Y. Liu and Z. Kang, *ACS Appl. Mater. Interfaces*, 2015, **7**, 10004–10012.
37 X. Ren, J. Liu, J. Ren, F. Tang and X. Meng, *Nanoscale*, 2015, **7**, 19641–19646.
38 S. Chen, Y. Wang, M. Zhong, D. Yu, C. Wang and X. Lu, *ACS Biomater. Sci. Eng.*, 2019, **5**, 1238–1246.
39 A. Sun, L. Mu and X. Hu, *ACS Appl. Mater. Interfaces*, 2017, **9**, 12241–12252.
40 T. Bhengu, T. Wood, M. Shumane and F. Tafesse, *Phosphorus, Sulfur Silicon Relat. Elem.*, 2019, **194**, 87–101.
41 H. Ming, Z. Ma, Y. Liu, K. Pan, H. Yu, F. Wang and Z. Kang, *Dalton Trans.*, 2012, **41**, 9526–9531.
42 W. Wang, Y. Li, L. Cheng, Z. Cao and W. Liu, *J. Mater. Chem. B*, 2014, **2**, 46–48.
43 B. De and N. Karak, *RSC Adv.*, 2013, **3**, 8286–8290.
44 Q. Xu, J. Zhao, Y. Liu, P. Pu, X. Wang, Y. Chen, C. Gao, J. Chen and H. Zhou, *J. Mater. Sci.*, 2015, **50**, 2571–2576.
45 Q. Xu, J. Wei, J. Wang, Y. Liu, N. Li, Y. Chen, C. Gao, W. Zhang and T. S. Sreeprased, *RSC Adv.*, 2016, **6**, 28745–28750.
46 J. Cheng, C.-F. Wang, Y. Zhang, S. Yang and S. Chen, *RSC Adv.*, 2016, **6**, 37189–37194.
47 Q. Xu, Y. Liu, R. Su, L. Cai, B. Li, Y. Zhang, L. Zhang, Y. Wang, Y. Wang, N. Li, X. Gong, Z. Gu, Y. Chen, Y. Tan, C. Dong and T. S. Sreeprasad, *Nanoscale*, 2016, **8**, 17919–17927.

48 R. Atchudan, T. N. J. I. Edison, D. Chakradhar, S. Perumal, J.-J. Shim and Y. R. Lee, *Sens. Actuators, B*, 2017, **246**, 497–509.
49 B. B. Chen, Z. X. Liu, H. Y. Zou and C. Z. Huang, *Analyst*, 2016, **141**, 2676–2681.
50 H. Li, Z. Kang, Y. Liu and S.-T. Lee, *J. Mater. Chem.*, 2012, **22**, 24230–24253.
51 H. C. Schniepp, J.-L. Li, M. J. McAllister, H. Sai, M. Herrera-Alonso, D. H. Adamson, R. K. Prud'homme, R. Car, D. A. Saville and I. A. Aksay, *J. Phys. Chem. B*, 2006, **110**, 8535–8539.
52 H. Yang, J. Zha, P. Zhang, Y. Qin, T. Chen and F. Ye, *Sens. Actuators, B*, 2017, **247**, 469–478.
53 Y. Yu, P. Ju, D. Zhang, X. Han, X. Yin, L. Zheng and C. Sun, *Sens. Actuators, B*, 2016, **233**, 162–172.
54 J. Fang, S. Zhuo and C. Zhu, *Opt. Mater.*, 2019, **97**, 109396.
55 W. Gao, Y. Zhou, C. Xu, M. Guo, Z. Qi, X. Peng and B. Gao, *Sens. Actuators, B*, 2019, **281**, 905–911.
56 P.-C. Hsu and H.-T. Chang, *Chem. Commun.*, 2012, **48**, 3984–3986.
57 R. Sanyal, X. Zhang, P. Chakraborty, S. Giri, S. K. Chattopadhyay, C. Zhao and D. Das, *New J. Chem.*, 2016, **40**, 7388–7398.
58 M. Garai, D. Dey, H. R. Yadav, A. R. Choudhury, N. Kole and B. Biswas, *Polyhedron*, 2017, **129**, 114–122.
59 V. Rajendiran, R. Karthik, M. Palaniandavar, H. Stoeckli-Evans, V. S. Periasamy, M. A. Akbarsha, B. S. Srinag and H. Krishnamurthy, *Inorg. Chem.*, 2007, **46**, 8208–8221.
60 F.-M. Feng, S.-L. Cai and F.-A. Liu, *J. Dispersion Sci. Technol.*, 2016, **37**, 352–359.
61 W. Jiang, B. Xu, Q. Lin, J. Li, F. Liu, X. Zeng and H. Chen, *Colloids Surf., A*, 2008, **315**, 103–109.
62 L. Gao, J. Zhuang, L. Nie, J. Zhang, Y. Zhang, N. Gu, T. Wang, J. Feng, D. Yang and S. Perrett, *Nat. Nanotechnol.*, 2007, **2**, 577.
63 H. Wei and E. Wang, *Anal. Chem.*, 2008, **80**, 2250–2254.
64 J. Shi, T. Yin and W. Shen, *Colloids Surf., B*, 2019, **178**, 163–169.
65 Y. Gao, K. Wu, H. Li, W. Chen, M. Fu, K. Yue, X. Zhu and Q. Liu, *Sens. Actuators, B*, 2018, **273**, 1635–1639.
66 G. Cao, D. Sun, T. Gu, Y. Dong and G.-L. Wang, *Biosens. Bioelectron.*, 2019, **145**, 111707.
67 G. Li, H. Fu, X. Chen, P. Gong, G. Chen, L. Xia, H. Wang, J. You and Y. Wu, *Anal. Chem.*, 2016, **88**, 2720–2726.
68 F. Yan, F. Zu, J. Xu, X. Zhou, Z. Bai, C. Ma, Y. Luo and L. Chen, *Sens. Actuators, B*, 2019, **287**, 231–240.
69 J. Du, Y. Zhao, J. Chen, P. Zhang, L. Gao, M. Wang, C. Cao, W. Wen and C. Zhu, *RSC Adv.*, 2017, **7**, 33929–33936.
70 Y. Zhang, Z. Xiao, F. Chen, Y. Ge, J. Wu and X. Hu, *Ultrason. Sonochem.*, 2010, **17**, 72–77.
71 M. A. Martínez, S. Ballesteros, C. Sánchez de la Torre, A. Sanchiz, E. Almarza and A. García-Aguilera, *J. Anal. Toxicol.*, 2004, **28**, 609–615.